Final version of this paper was published at
IEEE Transactions on Energy Conversion. 2023, 38(1), 170-179. ISSN 0885-8969.

A Novel Structure of Eddy Current Sensor for Speed Measurement of Rotating Shafts

Mehran Mirzaei, *Senior Member, IEEE,* Pavel Ripka, *Member, IEEE,*
and Vaclav Grim, *Member, IEEE*

***Abstract*—This paper presents a novel structure of an eddy current sensor for the measurement of rotational speed. The sensor has perpendicular configuration of excitation coil and pick up coil. Its maximum nonlinearity error is 0.15%. The excitation and pick coils are divided to two identical parts with coil span of 180 degrees. Various solid iron cylinders with different electrical and magnetic characteristics, one solid aluminum cylinder and one solid copper cylinder were used as the rotating shafts. A novel 2D analytical method in cylindrical coordinates is developed for fast parametric analysis of this sensor. 3D time stepping finite element method with consideration of the shaft motion is used for the performance analysis of eddy current sensor. The measurements of the speed sensor are performed at various frequencies and speeds and compared with the calculations for detailed analysis. The effects of rotating shaft materials are evaluated both in the measurements and the calculations.**

***Index Terms*— Analytical method, eddy current, finite element method, perpendicular coils, rotating shafts, speed sensor**

I. Introduction

THE speed and movement measurement is always a key issue in industrial and nonindustrial applications with motional parts. Control, maintenance, optimal energy consumption and management, and protection of any moving apparatus is feasible when precise device is utilized for the speed measurement [1]-[2]. Simplicity, reliability and robustness of speed measurement methodology are also considered beside its precision, when selecting or designing speed sensor for required applications [2]. Variation of magnetic reluctance or induced eddy current in salient conductive parts caused by translational or rotation motion can be sensed and utilized to measure speed [3], however, it is not a nondestructive method in all applications. The sensitivity of optical encoder and speed sensor to dust and dirt makes it less appropriate for all industrial applications.

Rotating apparatuses such as diesel mechanical engines and DC and induction machines have been backbone of industry since beginning of last century. Permanent magnet machines with NdFeB magnets become main competitor of DC and induction machines with superiority in higher efficiency and power density, especially for tractions and electrical vehicle applications. However, they suffer from using high cost and rare NdFeB magnets and their high sensitivity to the temperature and demagnetization. Therefore, induction machines can be a safer option for the traction in electrical vehicles [4]-[7], which need a robust and cost-effective speed sensor. Sensorless speed measurements have had recently magnificent developments with advantages of nonintrusive sensor installing process to the machine as no overhaul of the machine is required to install speed sensor on the rotating shaft inside the machine housing or if it is no access to the rotating shaft [8]-[9]. However, sensorless methods suffer from low accuracy at low speeds, electrical faulty conditions and very complicated required hardware [10]. Variable reluctance rotating resolvers can be used for the speed measurements with high accuracy and simple stationary part [11]-[13]. Nevertheless, moving part of resolver is attached to the shaft, which is not enough robust for the machines with high vibrating shaft loads.

Induced eddy current in the conductive objects has two components: transformer component caused by time variation of source fields and motional component caused by relative movement between conductive objects and excitation magnetic fields [14]. Motional component of induced eddy current causes asymmetricity of magnetic flux distribution in the conductive objects [15]-[16], which does not occur with transformer component of induced eddy current, for which the magnetic flux distribution is symmetric. The motional component of induced eddy current can cause additional losses and deteriorate machine performance [17]. Though, it can be utilized in eddy current brakes [18]-[19] and eddy current speed sensor as flowmeters [20]-[21]. A speed sensor using the fluxgate effect in an amorphous ring core to measure the field of motional eddy currents was presented in [22]. This is a rather complicated sensor with a high linearity error of approximately 5%. A Hall sensor using permanent magnet excitation was presented in [23], which shows poor offset stability. Linear speed measurements of solid conductive objects with eddy current speed sensors using motional component of induced eddy current for longitudinal and axisymmetric configurations were presented in [24]-[31], which shows excellent linearity versus speed for magnetic and nonmagnetic conductive moving objects [30]-[31]. Rotational speed measurements were shown

M. Mirzaei is with Czech Technical University, Prague, 16627, Czech Republic (e-mail: mirzameh@ fel.cvut.cz).
P. Ripka is with Czech Technical University, Prague, 16627, Czech Republic.
V. Grim is with Czech Technical University, Prague, 16627, Czech Republic.

in [32]-[33] using eddy current speed sensor with cost effective, nonintrusive, nondestructive and simple structure. The low nonlinearity error was shown in [30] and [31] for eddy current speed sensor, but the disadvantage of these sensors was low sensitivity.

A comprehensive calculation and measurements of a novel eddy current speed sensor with perpendicular excitation coils and pick up coils are presented in this paper. The new configuration of coils results in higher sensitivity. Detailed parametric analyses of speed sensor are performed using a novel 2D analytical calculations. 3D time stepping finite element method (FEM) is used to consider third dimension effects in the eddy current speed sensor and the results are compared with the measurements. The effects of rotating shaft material on sensitivity and linearity are evaluated. The sensitivity of new sensor is improved 6.5 times in comparison with the sensor in [33] with the same power consumption.

II. Structure and Theory of The Sensor

Fig. 1 shows 3D model of the eddy current speed sensor and rotating solid shaft. The excitation coils and pick up coils are perpendicularly positioned as shown in Fig. 1 and Fig. 2. The arrangement and polarity of the coils and their connections are presented in Fig. 2. The pick up coils have zero net flux linkage at zero speed due to the symmetric magnetic flux distribution as shown in Fig. 3 a). Rotating shaft speed causes asymmetric magnetic flux and nonzero net flux linkage for pick up coils, which can induce voltage in the pick up coils with AC excitation. The induced voltage in the pick up coils is proportional to the speed of rotating shaft and it could be therefore used as a speedmeter.

III. Analytical Modeling

2D analytical modelling in cylindrical coordinate system is performed in two steps to simplify the computation of the magnetic fields. The source field generated by excitation coils is calculated in the first step. The reaction field caused by induced eddy current in the solid rotating shaft is calculated in the second step.

A. Modeling of Fields for Excitation Coils

Only excitation coils are considered in the modeling for calculations of source fields generated by excitation coils. Three regions, e_1, e_2 and e_3 are considered in the computational model as shown in Fig. 2. Region, e_1 is air part beyond excitation coils ($r > r_{e\text{-}o}$), region, e_2 is excitation coils part ($r_{e\text{-}i} < r < r_{e\text{-}o}$) and region, e_3 corresponds to part inside the excitation coils ($r < r_{e\text{-}i}$). $r_{e\text{-}i}$ and $r_{e\text{-}o}$ are inner and outer radiuses of the excitation coils, respectively. The governing differential equations extracted from Maxwell equations are presented in (1) in cylindrical coordinate [14] and [32] versus magnetic vector potential, A_z for three regions, e_1, e_2 and e_3.

$$\frac{1}{r}\frac{\partial}{\partial r}\left(r\frac{\partial A_{z,e_1}}{\partial r}\right)+\frac{1}{r^2}\frac{\partial^2 A_{z,e_1}}{\partial \theta^2}=0$$

$$\frac{1}{r}\frac{\partial}{\partial r}\left(r\frac{\partial A_{z,e_2}}{\partial r}\right)+\frac{1}{r^2}\frac{\partial^2 A_{z,e_2}}{\partial \theta^2}=-\mu_0\cdot J_s$$

$$\frac{1}{r}\frac{\partial}{\partial r}\left(r\frac{\partial A_{z,e_3}}{\partial r}\right)+\frac{1}{r^2}\frac{\partial^2 A_{z,e_3}}{\partial \theta^2}=0 \quad (1)$$

where, J_s is the source current density in the coils. μ_0 is permeability of air.

The method of separation of variables (method of Fourier) is used to solve (1) [34]-[35]. Therefore, it is assumed that the magnetic fields are sinusoidal functions of time, and they change periodically in azimuthal direction with period length 2π. The solutions of (1) are presented in (2) with the form of sum of series, where m is harmonic order with odd integer numbers.

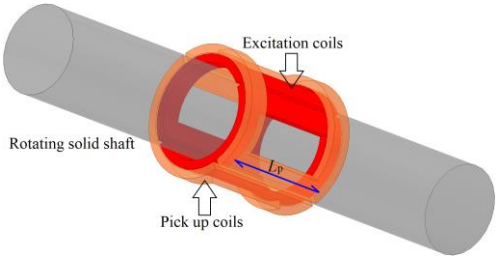

Fig. 1. 3D model of eddy current speed sensor and rotating solid shaft

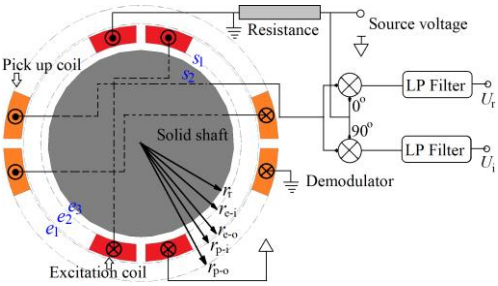

Fig. 2. 2D view of eddy current speed sensor, excitation coils and pick up coils and schematic model of connected lock in amplifier to the pick up coils and connected source voltage to the excitation coils

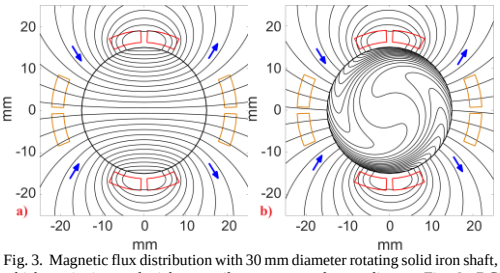

Fig. 3. Magnetic flux distribution with 30 mm diameter rotating solid iron shaft, which excitation and pick up coils are arranged according to Fig. 2, DC excitation using 2D analytical method – a) 0 speed, b) 3000 rpm

$$A_{z,e_1} = \sum_{m=\pm1,\pm3,\dots} \left(C_{e_1-1} r^{|m|} + C_{e_1-2} r^{-|m|}\right) \cdot e^{j(\omega t - m\theta)}$$
$$A_{z,e_2} = \sum_{m=\pm1,\pm3,\dots} \left(C_{e_2-1} r^{|m|} + C_{e_2-2} r^{-|m|} + \frac{\mu_0 J_{s,m}}{m^2-4} \cdot r^2\right) \cdot e^{j(\omega t - m\theta)}$$
$$A_{z,e_3} = \sum_{m=\pm1,\pm3,\dots} \left(C_{e_3-1} r^{|m|} + C_{e_3-2} r^{-|m|}\right) \cdot e^{j(\omega t - m\theta)}$$
$$J_{s,m} = \frac{2}{m\pi}\left(\cos\left(m\frac{\theta_{e-i}}{2}\right) - \cos\left(m\frac{\theta_{e-o}}{2}\right)\right) \cdot J_s$$
$$J_s = \frac{N_e I_e}{a_{we}}, \quad \omega = 2\pi f$$
$$a_{we} = \frac{(\theta_{e-o} - \theta_{e-i})}{4} \cdot (r_{e-o}^2 - r_{e-i}^2)$$

(2)

where, N_e, I_e and f are number of turns in excitation coil, current amplitude in the excitation coils and frequency. $\theta_{e\text{-}o}$ and $\theta_{e\text{-}i}$ are outer and inner span angles of the excitation coils in azimuthal direction. C_{e_1-1}, C_{e_1-2}, C_{e_2-1}, C_{e_2-2}, C_{e_3-1} and C_{e_3-2} are constants, which are calculated from the boundary conditions as follows:

$$B_{r,e_1}(r=\infty) = 0$$
$$B_{r,e_1}(r=r_{e-o}) = B_{r,e_2}(r=r_{e-o})$$
$$H_{\theta,e_1}(r=r_{e-o}) = H_{\theta,e_2}(r=r_{e-o})$$
$$B_{r,e_2}(r=r_{e-i}) = B_{r,e_3}(r=r_{e-i})$$
$$H_{\theta,e_2}(r=r_{e-i}) = H_{\theta,e_3}(r=r_{e-i})$$
$$B_{r,e_3}(r=0) = 0$$

(3)

where B_r and H_θ are radial component of magnetic flux density and azimuthal component of magnetic field strength.

B. Modeling of Fields for Solid Shaft

Only solid shaft is considered in the modeling for the calculations of the reaction fields of induced eddy currents. Two regions, s_1 and s_2, are considered in the computational model as shown in Fig. 2. Region s_1 is air part beyond rotating solid shaft with speed in rpm, n_r ($\omega_r = 2\pi n_r/60$) and region, s_2 is rotating solid shaft. Differential equations versus magnetic vector potential A_z are presented in (4).

$$\frac{1}{r}\frac{\partial}{\partial r}\left(r\frac{\partial A_{z,s_1}}{\partial r}\right) + \frac{1}{r^2}\frac{\partial^2 A_{z,s_1}}{\partial \theta^2} = 0$$
$$\frac{1}{r}\frac{\partial}{\partial r}\left(r\frac{\partial A_{z,s_2}}{\partial r}\right) + \frac{1}{r^2}\frac{\partial^2 A_{z,s_2}}{\partial \theta^2} = \mu_0\mu_r\sigma\left(\frac{\partial A_{z,s_2}}{\partial t} + \omega_r\frac{\partial A_{z,s_2}}{\partial \theta}\right)$$

(4)

Equation (5) presents the solutions of (4). I and K are Bessel functions.

$$A_{z,s_1} = \sum_{m=\pm1,\pm3,\dots} \left(C_{s_1-1} r^{|m|} + C_{s_1-2} r^{-|m|}\right) \cdot e^{j(\omega t - m\theta)}$$
$$A_{z,s_2} = \sum_{m=\pm1,\pm3,\dots} \left(C_{s_2-1} I(|m|, \gamma\cdot r) + C_{s_2-2} K(|m|, \gamma\cdot r)\right) \cdot e^{j(\omega t - m\theta)}$$
$$\gamma = \sqrt{j\mu_0\mu_r\sigma(\omega - m\cdot\omega_r)}, \quad \omega_r = 2\pi n_r/60$$

(5)

where μ_r, σ and n_r are relative magnetic permeability of shaft, electrical conductivity of shaft and rotating speed of shaft, respectively. C_{s_1-1}, C_{s_1-2}, C_{s_2-1} and C_{s_2-2} are constants, which are calculated from the following boundary conditions [30] and [34]:

$$B_{r,s_1}(r=\infty) = 0$$
$$B_{r,s_1}(r=r_r) + B_{r,e_3}(r=r_r) = B_{r,s_2}(r=r_r)$$
$$H_{\theta,s_1}(r=r_r) + H_{\theta,e_3}(r=r_r) = H_{\theta,s_2}(r=r_r)$$
$$B_{r,s_2}(r=0) = 0$$

(6)

B_{r,e_3} and H_{θ,e_3} are radial component of source flux density and azimuthal component of source magnetic field strength, which are calculated using (2). r_r is radius of rotating shaft.

C. Induced Voltage in the Pick up coils

The induced voltage in the pick up coils is calculated according to (7) and (8), where line integration of the magnetic vector potential is performed along axial direction [14]. Only the reaction fields are considered to calculate induced voltage as the source fields does not induce voltage in the pick up coils.

$$U_p = -\frac{d\Psi_p}{dt} = -j\omega 4N_p \oint A_{z,s_1} dl = -j\omega 4L_p N_p\left(A_{z,s_1}^{+} - A_{z,s_1}^{-}\right)$$

(7)

where L_p and N_p are mean axial length of pick up coils and number of turns in each pick up coil. A_{z,s_1}^{+} and A_{z,s_1}^{-} are average of magnetic vector potential over the cross-section areas of go (+) and return (-) coil sides, respectively (Fig. 2).

$$U_p = \frac{j\omega 4L_p N_p}{a_{wp}} \sum_{m=\pm1,\pm3,\dots} C_{K,0}$$
$$a_{wp} = \frac{(\theta_{p-o} - \theta_{p-i})}{4} \cdot \left(r_{p-o}^2 - r_{p-i}^2\right)$$

(8)

$$C_{K,0} = C_{K,1}\frac{4\sin\left(m\frac{\pi}{2}\right)}{m}\left(\cos\left(m\frac{\theta_{p-i}}{2}\right) - \cos\left(m\frac{\theta_{p-o}}{2}\right)\right)$$

(9)

$$C_{K,1} = C_{K,2}\frac{C_{K,3}-1}{C_{K,3}+1}\frac{r_{p-o}^{-|m|+2} - r_{p-i}^{-|m|+2}}{-|m|+2} r_r^{2|m|}$$

$$C_{K,2} = -\frac{\mu_0 J_{s,m}}{m^2-4}\left(\frac{1}{2}+\frac{1}{|m|}\right)\left(r_{e-o}^{-|m|+2} - r_{e-i}^{-|m|+2}\right)$$

$$C_{K,3} = \mu_r \frac{I(|m|, \gamma \cdot r_r)}{\frac{\gamma \cdot r_r}{|m|} \cdot I(|m|-1, \gamma \cdot r_r) - I(|m|, \gamma \cdot r_r)} \quad (10)$$

The magnetic flux distributions are shown for solid iron shaft at 125 Hz and zero speed and 3000 rpm using parameters in Table I is shown in Fig. 4. The magnetic flux distribution is symmetric at zero speed, but it becomes asymmetric at nonzero speed. Therefore, the voltage is induced in the pick up coils.

TABLE I
EDDY CURRENT SPEED SENSOR PARAMETERS

Par.		Par.	
r_r	15 mm	N_e	90
$r_{e\text{-}o}$	19 mm	N_p	105
$r_{e\text{-}i}$	16.2 mm	$\theta_{e\text{-}i}$	127.5 deg.
$r_{p\text{-}o}$	19.3 mm	$\theta_{e\text{-}o}$	175.1 deg.
$r_{p\text{-}i}$	22.2 mm	$\theta_{p\text{-}i}$	135.2 deg.
L_p	39 mm	$\theta_{p\text{-}o}$	175.8 deg.

D. Parametric Calculations

Fig. 5 shows induced voltage (absolute value) versus shaft speed curves for solid iron and copper shafts at current amplitude I_e = 150 mA. The speed range, n_r is ±3000 rpm. The analytical analyses are performed at 125 Hz, 250 Hz, 500 Hz and 750 Hz. The graphs of induced voltages versus speed have linear curve shapes, which shows suitability of eddy current sensor for rotating speed measurements. The sensitivity of the sensor, K_a (U_p=K_a·n_r) increases by 95% with increasing frequency from 125 Hz to 750 Hz for iron shaft, however, it decreases by 76% for copper shaft.

The influence of increasing frequency up to 1000 Hz is shown in Fig. 6: the induced voltage increases monotonically in iron shaft for different relative magnetic permeability, μ_r and decreases monotonically in nonmagnetic (aluminum and copper) shafts after 200 Hz. Fig. 7 shows sensor voltage to frequency ratio versus frequency, which is equivalent to the magnetic flux linkage of the pick up coils. The reduction rate of voltage to frequency ratio or flux linkage versus frequency is higher for nonmagnetic rotating shafts. The flux linkage in the pick up coils with nonmagnetic shaft decreases more as the flux penetration is less at higher frequencies.

The induced voltage for solid magnetic (iron) shaft versus conductivity for 1.0 - 10.0 MS/m range is shown in Fig. 8 a), which increases monotonically for different μ_r. It is depicted in Fig. 8 b) for 1.0 – 60.0 MS/m range for solid nonmagnetic (aluminum, copper or brass) shafts with a peak value, which depends on the conductivity of the shaft. The lower relative permeability, μ_r causes higher induced voltage for solid iron shaft as shown in Fig. 5 and Fig. 8.

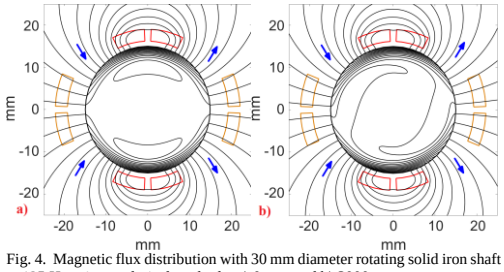

Fig. 4. Magnetic flux distribution with 30 mm diameter rotating solid iron shaft at 125 Hz using analytical method – a) 0 rpm and b) 3000 rpm

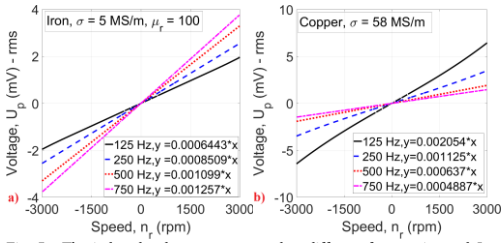

Fig. 5. The induced voltage versus speed at different frequencies and I_e = 150 mA – a) solid iron shaft, b) solid copper shaft

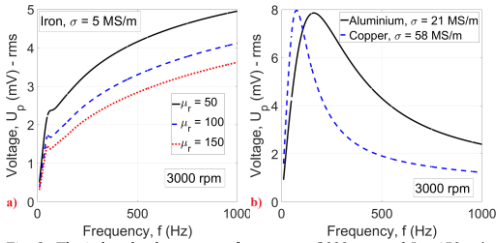

Fig. 6. The induced voltage versus frequency at 3000 rpm and I_e = 150 mA – a) solid iron shaft with different relative permeability, b) solid copper and aluminum shafts

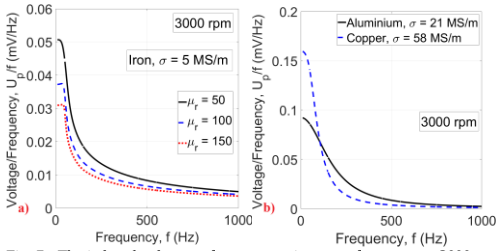

Fig. 7. The induced voltage to frequency ratio versus frequency at 3000 rpm and I_e = 150 mA – a) solid iron shaft with different relative permeability, b) solid copper and aluminum shafts

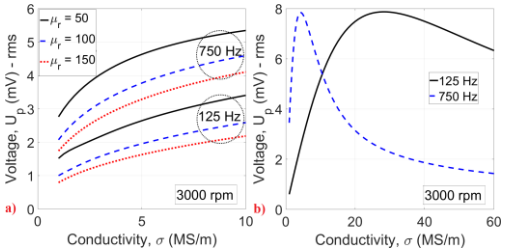

Fig. 8. The induced voltage versus shaft conductivity with 125 Hz and 750 Hz and at 3000 rpm and I_e = 150 mA - a) solid iron (magnetic) shaft with different relative permeability, b) solid nonmagnetic shaft

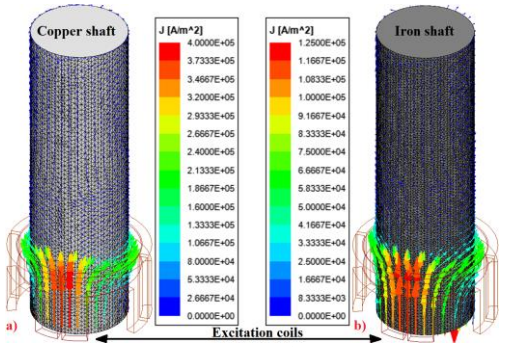

Fig. 9. Eddy current distributions on the shaft at 3000 rpm, 250 Hz and and I_e = 150 mA – a) copper shaft, b) iron shaft

IV. 2D AND 3D FEM ANALYSES

2D and 3D FEM are considered for further analysis of the eddy current speed sensor using Maxwell/Ansys software. Time stepping approach is used for the modeling of the sensor. The motion of the rotor is modeled with sliding surface method [36]-[39]. Only half of the model in axial direction is considered in 3D analysis due to the symmetry in axial direction as shown in Fig. 9. Eddy current distribution on the surface of copper and iron shafts is depicted in Fig. 9, which shows two poles configuration. The current density value is higher on the surface of the copper shaft at 250 Hz.

Table II shows comparison between 2D analytical and 2D/3D FEM for absolute value of the induced voltage. The simulations are performed at 3000 rpm with excitation frequencies, 250 Hz and 750 Hz. 2D analytical results match excellent with 2D FEM results, which shows high accuracy of the proposed analytical method. 3D FEM results are higher as 3rd dimension or end effects are considered in 3D modeling. The eddy current distribution is intrinsically 3D [40]-[41] and 2D modeling can not be accurate as 3D calculations. However, 3D time stepping FEM is very time consuming and it is not therefore suitable for time efficient parametric calculations.

Fig. 10. The experimental set up – DC motor as a prime mover, solid rotating shaft and eddy current speed sensor

TABLE II
COMPARISON BETWEEN 2D ANALYTICAL AND 2D/3D FEM RESULTS FOR SENSOR VOLTAGES – RMS VALUES

Shaft – 3000 rpm 150 mA		Voltage (mV)		
		2D Analytical	2D FEM	3D FEM
Copper	250 Hz	3.49	3.47	4.05
σ= 58.0 MS/m	750 Hz	1.45	1.46	1.97
Aluminum	250 Hz	7.07	6.89	6.70
σ= 21.0 MS/m	750 Hz	3.0	3.01	3.41
Iron, μ_r=100	250 Hz	2.53	2.54	4.21
σ= 5.0 MS/m	750 Hz	3.76	3.75	4.46

TABLE III
CONDUCTIVITIES OF SHAFTS

Material	Conductivity (MS/m)
Copper	56.66
Aluminum	20.97
Iron1	5.44
Iron2	5.24
Iron3	4.51

V. EXPERIMENTAL RESULTS

Fig. 10 shows experimental setup including a DC motor as prime mover, solid shaft and eddy current speed sensor with dimensions mentioned in Table I. The measurements are performed at speed range ±3000 rpm and various frequencies. Three various solid iron shafts, Iron1, Iron2 and Iron3 with different conductivities, one aluminum shaft and one copper shaft are used for the rotating speed measurements. Table III shows measured materials conductivities for copper, aluminum and three iron shafts (Iron1, Iron2 and Iron3).

An absolute angle sensor based on giant magnetoresistive effect is used to measure reference speed value utilizing magnetic field of a permanent magnet, which is mounted on the non-drive end shaft of prime mover.

Okomentoval(a): [RP1]: Please specify the sensor type

A lock in amplifier is used for the precise measurements of real, U_r and imaginary, U_i components of the induced voltage. The reference signal for lock in amplifier is the current in the excitation coil, which is measured using voltage on the resistance in series with excitation coil. The excitation coil is connected to a signal generator with internal resistance 50 Ω and voltage amplitude 10 V. The schematic view of lock in amplifier and signal generator connected to pick up coils and excitation coil is shown in Fig. 2. The total voltage $U_{p,a}$ of pick up coils is calculated as $U_{p,a} = \sqrt{U_r^2 + U_i^2}$.

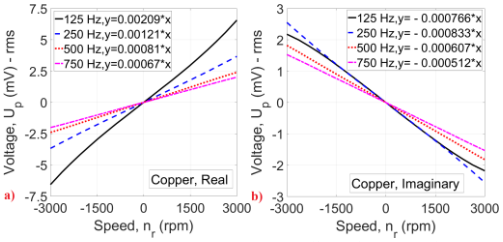

Fig. 11. The induced voltage versus speed at different frequencies for copper shaft - a) real component, b) imaginary component

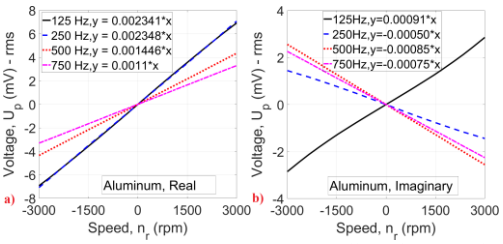

Fig. 12. The induced voltage versus speed at different frequencies for aluminum shaft - a) real component, b) imaginary component

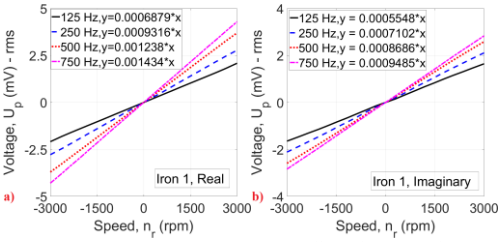

Fig. 13. The induced voltage versus speed at different frequencies for Iron 1 shaft - a) real component, b) imaginary component

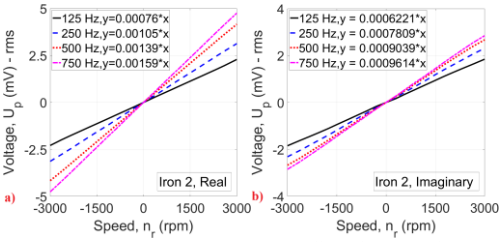

Fig. 14. The induced voltage versus speed at different frequencies for Iron 2 shaft - a) real component, b) imaginary component

A. Sensitivity Analysis

The experiments are performed at various excitation frequencies, 125 Hz, 250 Hz, 500 Hz and 750 Hz. The real and imaginary components of pick up coils voltage are shown in Fig. 11 – Fig. 15 for various shafts. The graphs show different tendencies versus speed, which strongly depends on the material properties.

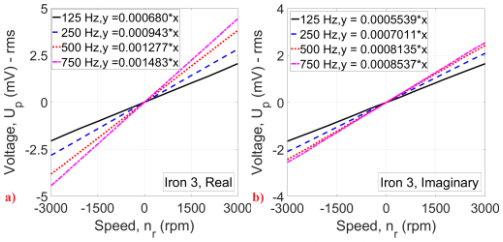

Fig. 15. The induced voltage versus speed at different frequencies for Iron 3 shaft - a) real component, b) imaginary component

TABLE IV
CURRENT OF EXCITATION COILS – RMS VALUE

Material	125 Hz	250 Hz	500 Hz	750 Hz
Copper	112 mA	112 mA	111 mA	111 mA
Aluminum	112 mA	112 mA	111 mA	111 mA
Iron1	112 mA	112 mA	111 mA	109 mA
Iron2	112 mA	112 mA	111 mA	109 mA
Iron3	112 mA	112 mA	111 mA	109 mA

TABLE V
SENSITIVITY OF THE SENSOR – REAL COMPONENT

K_r, μV/rpm	125 Hz	250 Hz	500 Hz	750 Hz
Copper	2.09	1.21	0.81	0.67
Aluminum	2.341	2.348	1.446	1.10
Iron1	0.688	0.932	1.238	1.434
Iron2	0.760	1.05	1.39	1.59
Iron3	0.680	0.943	1.277	1.483

TABLE VI
SENSITIVITY OF THE SENSOR – IMAGINARY COMPONENT

K_i, μV/rpm	125 Hz	250 Hz	500 Hz	750 Hz
Copper	-0.766	-0.833	-0.607	-0.512
Aluminum	0.91	-0.50	-0.85	-0.75
Iron1	0.555	0.710	0.869	0.949
Iron2	0.622	0.781	0.904	0.961
Iron3	0.554	0.701	0.814	0.854

The induced voltage is higher for copper shaft in comparison with aluminum shaft at 125 Hz because of higher conductivity. However, it is vice versa at higher frequencies due to the lower magnetic flux penetration depth and higher skin effects. The measured current of the excitation coil is presented in Table IV. It is less at higher frequencies as reactance voltage excitation coil is higher, therefore, the current decreases for applied source voltage with constant amplitude.

The sensitivities of the sensor for real and imaginary components of voltage are presented in Table V and Table VI (U_r=K_r·n_r and U_i=K_i·n_r). The sensitivity corresponding to the imaginary component of voltage, K_i is negative for copper and aluminum shafts at higher frequencies. The sensitivities for copper and aluminum shafts decrease at higher frequencies as magnetic flux penetration depth decreases because of higher skin effects.

The sensitivities K_r for real component are higher than sensitivities K_i for imaginary component for rotating iron shafts, and they increase with increasing frequency. The real component sensitivity, K_r increases over 100% when frequency increases sixfold from 125 Hz to 750 Hz. The imaginary

component sensitivity, K_i increases about 55% to 71% with increasing frequency from 125 Hz to 750 Hz.

The shafts Iron1 and Iron3 have different conductivities (Table III). However, the real component sensitivities, K_r are matching at different frequencies (Table V). This is different for shaft Iron2 despite it has the same conductivity as shaft Iron1; this is caused by its different relative magnetic permeability, μ_r. The imaginary component sensitivities, K_i are similar for shafts Iron1 and Iron2 at higher frequencies. It shows that the effect of changing relative magnetic permeability is lower at higher frequencies for imaginary component of voltage. Shaft Iron2 has highest sensitivities for K_r and K_i.

B. Nonlinearity Error Analysis

The nonlinearity error, E is calculated based on the deviation of the sensor output voltages, $U_p(n_r)$ from linear fitted function, $f_l(n_r)$ of the voltage versus speed, n_r curve over measured speeds range, $n_r = \pm 3000$ rpm. It is presented in the percentage of the full scale:

$$E = \frac{U_p(n_r) - f_l(n_r)}{U_{p-max}(3000\ \text{rpm})} \cdot 100\ \% \quad (11)$$

The nonlinearity errors for real and imaginary components of voltage are depicted in Fig. 16 and Fig. 17 for nonmagnetic copper and aluminum shafts and in Fig. 18 – Fig. 20 for magnetic shafts, Iron1, Iron2 and Iron3. The imaginary component of voltage curves versus speed shows high linearity characteristic for copper shaft with 0.265% error and aluminum shaft with 0.2% error. The real component of voltage curves versus speed has higher linearity for iron shafts with minimum nonlinearity error as low as 0.15%.

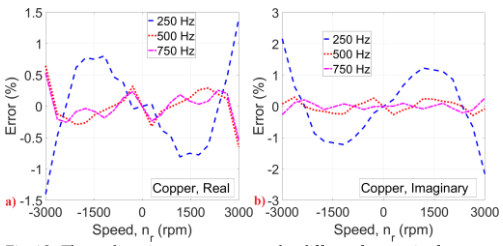

Fig. 16. The nonlinearity error versus speed at different frequencies for copper shaft - a) real component, b) imaginary component

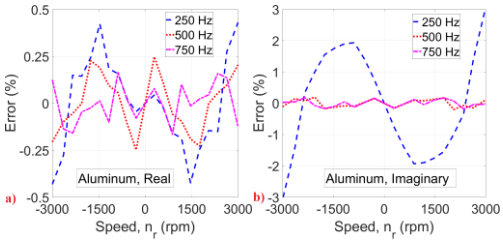

Fig. 17. The nonlinearity error versus speed at different frequencies for aluminum shaft - a) real component, b) imaginary component

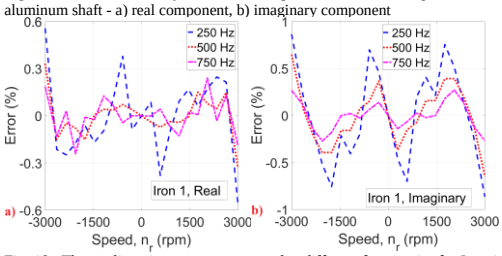

Fig. 18. The nonlinearity error versus speed at different frequencies for Iron 1 shaft - a) real component, b) imaginary component

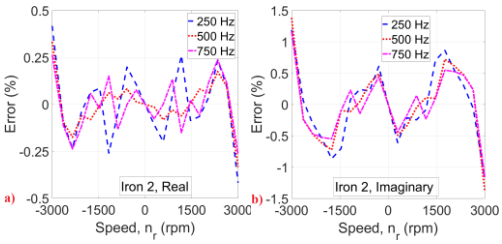

Fig. 19. The nonlinearity error versus speed at different frequencies for Iron 2 shaft - a) real component, b) imaginary component

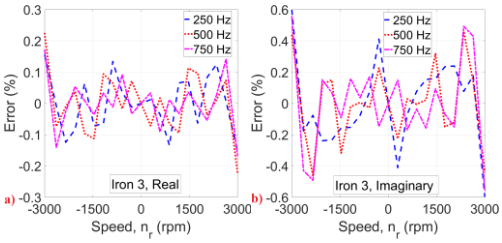

Fig. 20. The nonlinearity error versus speed at different frequencies for Iron 3 shaft - a) real component, b) imaginary component

C. Comparison between Experimental and 3D FEM

The comparison between 3D FEM calculations using current values in Table VII and experimental results for absolute value of the sensor voltage are presented in Table VII. The difference between 3D FEM and measurement is maximum 6 % for nonmagnetic shafts, which shows appropriate accuracy of 3D FEM modeling and design for rotational eddy current speed sensor. 3D FEM modeling is made with different values of μ_r as shown in Table VII for iron shafts. We estimated μ_r to be about 200 for shaft Iron1 and 150 and 200 for shafts Iron2 and Iron3, respectively. The shaft Iron2 has lowest relative magnetic permeability, which causes higher pick up coil voltage and sensitivity for the eddy current speed sensor. 3D simulations show the same outcomes for material effect as the experimental results and 2D analytical modeling. The eddy current loss in the solid shafts is only about 10 mW at 250 Hz and 750 Hz for all shafts.

TABLE VII
COMPARISON BETWEEN 3D FEM AND EXPERIMENTAL RESULTS FOR SENSOR VOLTAGES – RMS VALUES

Shaft – 3000 rpm, 250 Hz		Voltage (mV) 3D FEM	Voltage (mV) Experimental
Copper		4.28 (94.0%)	4.55 (100%)
Aluminum		7.08 (98.1%)	7.22 (100%)
Iron1	μ_r=75	4.92 (139.4%)	3.53 (100%)
	μ_r=125	4.25 (120.3%)	
	μ_r=175	3.83 (108.6%)	
Iron2	μ_r=75	4.88 (123.9%)	3.94 (100%)
	μ_r=125	4.22 (107.0%)	
	μ_r=175	3.81 (96.7%)	
Iron3	μ_r=75	4.71 (133.2%)	3.54 (100%)
	μ_r=125	4.09 (115.5%)	
	μ_r=175	3.71 (104.9%)	

VI. DISCUSSIONS

The simple structure of the sensor decreases the price and maintenance of the speed sensor. The proposed eddy current speed sensor does not utilize additional part or gear to be mounted on the rotating shaft unlike variable reluctance and optical speed sensors, tachometers and resolvers, which makes it more fault tolerant against mechanical failure and to be mechanically more robust especially at high speeds. The sensor shows high linearity characteristics with nonlinearity error of 0.15%, which is quite lower compared to a commercial magnetic speed sensor with a tachometer configuration with a 1% nonlinearity error [42]. The sensitivity of the sensor can be easily improved by increasing number of turns in excitation and pick up coils using thinner wires, which is only limited by stray capacitance of the coils and resonance frequency.

The rotating shaft eccentricity could influence the sensor performance. Therefore, the effect of eccentricity is evaluated using 2D FEM. The analysis with 0.5 mm eccentricity is considered, which is about 41.7% of the gap between shaft and excitation coils, $g = r_{e\text{-}i} - r_r = 1.2$ mm. Such extreme eccentricity causes only 1.8% and 0.6% errors for solid iron and solid aluminum shafts, respectively. Using a nonmagnetic cylindrical shell on solid iron rotating shaft can decrease the eccentricity error for solid iron shaft, which also increases the sensitivity of the eddy current speed sensor [32]-[33].

The temperature of rotating shafts changes the conductivity σ and relative magnetic permeability μ_r as shown in Fig. 8, which affects the induced voltage of the speed sensor. Therefore, the temperature compensation is required to stabilize the sensor performance. Using nonmagnetic shell on the solid iron shaft can minimize the effects of μ_r changes on the sensor sensitivity as presented in [32]-[33]. The conductivity and relative magnetic permeability of the rotating shafts can be also estimated using nondestructive methods, for example, multifrequency electromagnetic and phase signature approaches [43]-[44]. They can be later utilized for the recalibration of the sensor at different shaft temperatures. As both real and imaginary components of the sensor voltage versus speed show highly linear characteristics, one component can be utilized as a speedmeter and another component for temperature compensation. The eddy current speed sensor can be also operated with double or triple excitation frequencies, which helps to utilize the induced voltages corresponding to second or third frequencies for eccentricity and temperature compensations beside using the induced voltage corresponding to first frequency for speedmeter.

The real and imaginary components of the sensor voltage or voltage amplitude and its phase angle are measured. As real, U_r and imaginary, U_i components of sensor voltage versus speed have high linearity, the absolute value of induced voltage, $U_{p,a} = \sqrt{U_r^2 + U_i^2}$ could be also utilized for the speed measurement and the phase is used to detect the speed polarity similar as for LVDT sensors. The linearity of the sensor depends on the excitation frequency, maximum speed range and material of rotating shaft. Operating the sensor at higher excitation frequencies helps to improve its. The sensitivity decreases considerably for nonmagnetic shafts at higher frequencies. Therefore, a frequency bandwidth should be considered based on compromise between linearity and sensitivity for nonmagnetic shafts. The sensitivity of the sensor increases monotonically with frequency for magnetic iron shafts. In this case the maximum excitation frequency is limited by the resonance frequency of the sensor coils.

VII. CONCLUSION

A novel configuration of eddy current sensor to measure rotating speed of conductive metallic shafts was presented. The newly developed 2D analytical modeling was used for parametric analysis. The advantage of 2D analytical modeling is fast calculation and less numerical errors, which gives an advantage over 2D and 3D FEM especially at high frequencies and high speeds. 3D FEM was utilized to evaluate experimental results and precise modeling of eddy current speed sensor with consideration of 3D model of speed sensor. It can be used for further design optimization of the sensor.

The effects of materials for the rotating shaft were assessed to evaluate eddy current speed sensor parameters versus electrical conductivity and relative magnetic permeability for iron shafts. It has been shown that rotating shaft material effects are considerable. Higher sensitivity can be achieved with lower relative magnetic permeability and higher conductivity for solid iron shafts.

The designed sensor shows excellent linearity with maximum nonlinearity about 0.15%. Perpendicular configuration of excitation coils and pick up coils increases sensitivity of eddy current speed sensor as it maximizes the efficient flux linkage of pick up coils caused by motional component of induced eddy current in solid conductive shaft of eddy current speed sensor.

REFERENCES

[1] Z. Xiao, Q. Wang, P. Sun, B. You, and X. Feng, "Modeling and energy-optimal control for high-speed trains," *IEEE Trans. Transportation Electrification*, vol. 6, no. 2, pp. 797-807, June 2020, DOI: 10.1109/TTE.2020.2983855

[2] S. F. Amirov and K. A. Sattarov, "Inductive sensors of angular acceleration," in *Proc. ICIEAM*, Sochi, Russia, 2020, DOI: 10.1109/ICIEAM48468.2020.9112045

[3] J. Rickman, "Eddy current turbocharger blade speed detection", *IEEE Trans. Mag.*, vol. 18, no. 5, pp. 1014-1021, Sep. 1982, DOI: 10.1109/TMAG.1982.1061962
[4] T.-V. Tran, E. Negre, K. Mikati, P. Pellerey and B. Assaad, "Optimal design of TEFC induction machine and experimental prototype testing for city battery electric vehicle," *IEEE Trans. Ind. Appl.*, vol. 56, no. 1, pp. 635-643, Jan./Feb. 2020
[5] N. Zhao and N. Schofield, "An induction machine design with parameter optimization for a 120-kW electric vehicle," *IEEE Trans. Transp. Electrif.*, vol. 6, no. 2, pp. 592-601, June 2020
[6] Y. Sadali, K. Kondo K. Aiso, K. Fujimoto, S. Makishima, Y. Nakashima and T. Yamaguchi, "Identifying the optimal induction motor design for increased power density in commuter railway use through loss analysis," 2021 *IEEE 12th Energy Conversion Congress & Exposition* - Asia (ECCE-Asia), pp. 1187-1192, 24-27 May 2021
[7] H. S. J. Juanchi, A. Chiba and M. Kobayashi, "Performance evaluation of a nine-phase induction motor using finite element analysis," 2020 *23rd International Conference on Electrical Machines and Systems* (ICEMS), pp. 1472-1477, 24-27 Nov. 2020
[8] M. Comanescu, "Design and implementation of a highly robust sensorless sliding mode observer for the flux magnitude of the induction motor," *IEEE Trans. Energy Conversion*, vol. 31, no. 2, pp. 649-657, June 2016, DOI: 10.1109/TEC.2016.2516951
[9] M. Chirindo , M. A. Khan, and P. Barendse, "Analysis of Non-Intrusive Rotor Speed Estimation Techniques for Inverter-Fed Induction Motors," *IEEE Trans. Energy Conversion*, vol. 36, no. 1, pp. 338-347, June 2021, DOI: 10.1109/TEC.2020.3007409
[10] C. D. Tran, P. Palacky, Ma. Kuchar, P. Brandstetter and B. H. Dinh "Current and speed sensor fault diagnosis method applied to induction motor drive," *IEEE Access*, vol. 9, pp. 38660 - 38672, 2021, DOI: 10.1109/ACCESS.2021.3064016
[11] L. Sun, Z. Luo, K. Wang, R. Cao, and S. Ding, "A stator-PM resolver with field modulation principle," *IEEE Trans. Energy Conv*., vol. 36, no. 1, pp. 159 – 172, March 2021.
[12] X. Ge, and Z. Q. Zhu, "A novel design of rotor contour for variable reluctance resolver by injecting auxiliary air-gap permeance harmonics," *IEEE Trans. Energy Conv*., vol. 31, no. 1, pp. 345-353, March 2016.
[13] X. Ge, Z. Q. Zhu, R. Ren, and J. T. Chen, "A novel variable reluctance resolver with nonoverlapping tooth–coil windings," *IEEE Trans. Energy Conv*., vol. 3., no. 2, pp. 784-794, June 2015.
[14] K. R. Davey, "Analytic analysis of single- and three-phase induction motors," *IEEE Trans. Magn.*, vol. 34, no. 5, pp. 3721–3727, Sep. 1998.
[15] D. Marcsa and M. Kuczmann, "Comparison of the A^*-A and T, Φ-Φ formulations for the 2-D analysis of solid-rotor induction machines," *IEEE Trans. Magn.*, vol. 45, no. 9, pp. 3329–3333, Sep. 2009.
[16] V. Raisanen, S. Suuriniemi, S. Kurz, and L. Kettunen, "Rapid computation of harmonic eddy-current losses in high-speed solid-rotor induction machines," *IEEE Trans. Energy Conversion*, vol. 28, no. 3, pp. 782-790, Sept. 2013
[17] G. Lv, D. Zeng, and T. Zhou, "Analysis of secondary losses and efficiency in linear induction motors with composite secondary based on space harmonic method," *IEEE Trans. Energy Conversion*, vol. 32, no. 4, pp. 1583-1591, Dec. 2017
[18] J. Bigeon, J. Sabonnadiere, and J. Coulomb, "Finite element analysis of an electromagnetic brake," *IEEE Trans. Magnetics*, vol. 19, no. 6, pp. 2632-2634, 1983
[19] D. Albertz, S. Dappen, and G. Henneberger, "Calculation of the 3D non-linear eddy current field in moving conductors and its application to braking systems," *IEEE Trans. Magnetics*, vol. 32, no. 3, pp. 768-771, 1996
[20] J. A. Shercliff, *The Theory of Electromagnetic Flow Measurement*, Cambridge, U.K.:Cambridge Univ. Press, 1962
[21] C. C. Feng, W. E. Deeds, C. V. Dodd, "Analysis of eddy-current flowmeters," *J. Appl. Phys*., vol. 46, no. 7, pp. 2935-2940, 1975
[22] T. Sonoda, R. Ueda, K. Fujitani, T. Irisa, and S. Tatata, "DC magnetic field type eddy current speed sensor detecting cross magnetization field with amorphous core", *IEEE Trans. Magn.*, vol. MAG-21, no. 5, pp. 1732-1734, Sep. 1985
[23] E. Cardelli, A. Faba, and F. Tissi, "Contact-less speed probe based on eddy currents," IEEE Trans. Magn., vol. 49, no. 7, pp. 3897–3900, Jul. 2013.
[24] N. Takehira, A. Tanaka, K. Toda, "Analysis of a speed-meter utilizing eddy current effect," *The Trans. Inst. Elect. Eng. Japan. A*, vol. 97, no. 9, pp. 457-464, Sept. 1977
[25] N. Takehira, A. Tanaka, "Analysis of a transmitted type speed-meter utilizing eddy current effect," *The Trans. Inst. Elect. Eng. Japan. A*, vol. 100, no. 9, pp. 483-490, Sept. 1980
[26] A. Tanaka, N. Takehira, "Eddy-current speed meter using Galvanomagnetic devices," *The Trans.* Inst. *Elect. Eng. Japan. A*, vol. 106, no. 6, pp. 267-274, June 1986
[27] N. Takehira and A. Tanaka, "Analysis of a perpendicular-type eddy-current speed meter," *IEE Proc. A Physical Sci., Meas. Instrum., Manage*. Edu. Rev., vol. 135, no. 2, pp. 89–94, Feb. 1988.
[28] T. Itaya, K. Ishida, A. Tanaka, N. Takehira, and S. Yamamoto, "Analysis of an eddy current speed meter by rectangular coil system," *IEEJ Trans. Fundamentals Mater*., vol. 133, no. 8, pp. 416–423, Jan. 2013.
[29] K. Ishida, T. Itaya T, A. Tanaka A, N. Takehira, "Exact analysis of a linear velocity sensor," *IEEE Trans. Inst. & Meas.*, vol. 70, 6002106, 2021
[30] M. Mirzaei, and P. Ripka, "A linear eddy current speed sensor with a perpendicular coils configuration," *IEEE Transactions on Vehicular Technology*, vol. 70, no. 4, pp. 3197 - 3207, April 2021
[31] M. Mirzaei, P. Ripka, and V. Grim, "A novel eddy current speed sensor with a Ferrite E-core," *IEEE Magnetics Letters*, vol. 11, 8102905, 08 May 2020
[32] M. Mirzaei, P. Ripka, J. Vyhnanek, A. Chirtsov and V. Grim, "Rotational eddy current speed sensor," *IEEE Trans. Mag.*, vol. 55, no. 9, 4003710, Sept. 2019
[33] M. Mirzaei, P. Ripka, V. Grim, and A. Chirtsov, "Design and optimization of an eddy current speed sensor for rotating rods," *IEEE Sens. J.*, vol. 20, no. 20, pp. 12241-12251, June 2020
[34] K.J. Binns, P.J. Lawrenson, and C.W. Trowbridge, *The Analytical and Numerical Solutions of Electric and Magnetic Fields*, Published by John Wiley & Sons Ltd., 1992
[35] M. N. O. Sadiku, *Numerical Techniques in Electromagnetics*, Second Edition, July 12, 2000 by CRC Press, Textbook
[36] P. Zhou, Z. Badics, D. Lin, and Z. J. Cendes, "Nonlinear T-Ω formulation including motion for multiply connected 3-D problems," *IEEE Trans. Mag.*, vol. 44, no. 6, pp. 718-721, June 2008
[37] C. Lu, P. Zhou, D. Lin, B. He, and D. Sun, "Multiply connected 3-D transient problem with rigid motion associated with T-Ω formulation," *IEEE Trans. Mag.*, vol. 50, no. 2, 7011004, Feb 2014
[38] B. He, C. Lu , and P. Zhou, "A hybrid parallel method for 3-D nonlinear periodic eddy current problems with motions," *IEEE Trans. Mag.*, vol. 54, no. 3, 7000704, March 2018
[39] D. Rodger, "Modeling movement in electrical machines," *IEEE Trans. Mag.*, vol. 57, 8105504, 2021
[40] J. P. Sturgess and T. W. Preston, "An economic solution for 3-D coupled electromagnetic and thermal eddy current problems," *IEEE Trans. Mag*., vol. 28, no. 2, pp. 1267-1270, March 1992
[41] M. Jagiela and T. Garbiec, "Evaluation of rotor-end factors in solid-rotor induction motors," *IEEE Trans. Mag.*, vol. 48, no. 1, pp. 137-142, Jan. 2012
[42] Handheld Tachometer. Accessed: May. 18, 2022. [Online]. Available:https://www.onosokki.co.jp/English/hp_e/whats_new/Catalog/PDF/digital_tachometers.pdf
[43] M. Lu, Y. Xie, W. Zhu, A. Peyton, and W. Yin, "Determination of the magnetic permeability, electrical conductivity, and thickness of Ferrite metallic plates using a multifrequency electromagnetic sensing system," *IEEE Trans. Inds. Informatics*, vol. 15, no. 7, pp. 4111-4119, July 2019
[44] M. Lu , R. Huang, W. Yin, Q. Zhao, and Anthony Peyton, "Measurement of permeability for Ferrous metallic plates using a novel lift-off compensation technique on phase signature," *IEEE Sensors J*., vol. 19, no. 17, pp. 7440-7446, Sept. 2019